

ARTICLE OPEN

Laser-induced hierarchical carbon patterns on polyimide substrates for flexible urea sensors

Emil R. Mamleyev¹, Stefan Heissler², Alexei Nefedov^{1,2}, Peter G. Weidler², Nurdiana Nordin¹, Vladislav V. Kudryashov³, Kerstin Länge¹, Neil MacKinnon¹ and Swati Sharma¹

Thermochemical decomposition of organic materials under heat-treatment in the absence of oxygen, known as the pyrolysis process, is often employed to convert micro and nano patterned polymers into carbon structures, which are subsequently used as device components. Pyrolysis is performed at ≥ 900 °C, which entails substrate materials with a high thermal stability that excludes flexible, polymeric substrates. We use optimized laser radiation to pattern graphitic carbon structures onto commercially available polyimide (Kapton) sheets in the micrometer to millimeter scale by inducing a localized, rapid pyrolysis, for the fabrication of flexible devices. Resulting laser carbon films are electrically conductive and exhibit a high-surface area with a hierarchical porosity distribution along their cross-section. The material is obtained using various combinations of laser parameters and pyrolysis environment (oxygen-containing and inert). Extensive characterization of laser carbon is performed to understand the correlation between the material properties and laser parameters, primarily fluence and power. A photochemical carbonization mechanism based on the plume formation is proposed. Further, laser carbon is used for the fabrication of enzymatic, pH-based urea sensors using two approaches: (i) direct urease enzyme immobilization onto carbon and (ii) electrodeposition of an intermediate chitosan layer prior to urease immobilization. This flexible sensor is tested for quantitative urea detection down to 10^{-4} M concentrations, while a qualitative, color-indicative test is performed on a folded sensor placed inside a tube to demonstrate its compatibility with catheters. Laser carbon is suitable for a variety of other flexible electronics and sensors, can be conveniently integrated with an external circuitry, heating elements, and with other microfabrication techniques such as fluidic platforms.

npj Flexible Electronics (2019)3:2; <https://doi.org/10.1038/s41528-018-0047-8>

INTRODUCTION

Conversion of micro and nano patterned polymer structures into carbon via pyrolysis is a widespread technique for the fabrication of graphitic carbon-based devices.^{1,2} This process is typically performed at ≥ 900 °C, such that the polymer undergoes a thermochemical decomposition and yields carbon with a characteristic dimensional shrinkage. The properties of such carbons are similar to those of glassy (IUPAC name: glass-like) carbon,^{1,2} which are attributed to a complex three-dimensional graphene network that constitutes the material.^{3–5} Carbon obtained from pyrolysis below 900 °C does not feature the desired graphenic network,⁶ therefore, its mechanical strength as well as electrical conductivity are compromised. Consequently, the elevated temperatures are essential for obtaining device-friendly carbon, which limit this process to substrate materials with a high thermal stability, such as silicon. In other words, patterning pyrolytic carbon onto flexible polymer substrates remains a challenge.

Laser-induced carbonization of polyimide (e.g., its commercially available derivative, Kapton) has been attempted for its conversion into a porous carbon material that is useable in devices.^{7–10} Initial observations were reported in the framework of polymer ablation,⁷ where the carbonaceous residue was considered undesirable. Further investigations were optimized to produce

carbon with a superior electrical conductivity using UV radiation with a nanosecond pulse or continuous wave.^{11,12} A combination of photochemical and photothermal mechanisms was proposed for such a conversion, which was supported by a model of single photon and multiphoton absorbance of chromophores;¹¹ later also confirmed by diffuse reflectance infrared (IR) Fourier transform studies.¹³ Eventually, the carbonization of Kapton was also carried out using IR¹⁴ and femto-second¹⁵ lasers. Importantly, the carbonization mechanism is expected to drastically vary in the case of each laser type owing to the fact that both polyimide and carbon exhibit different transmittance in different laser wavelengths. The heat generated during the process, as well as the microstructure and surface properties of the resulting carbon are strongly influenced by the laser power, fluence, speed, and pyrolysis environment, in addition to the wavelength. Since this technology is in its initial development phase, occasional dissimilarities in the nomenclature are also encountered. For example, essentially the same material is designated as glassy carbon,¹⁶ laser-scribed graphene^{17–19} and laser-induced graphene^{20–22} in various studies. The increasing interest in laser carbon aimed at flexible device fabrication has created a compelling need for the optimization of laser parameters, followed by a detailed characterization of the resulting material

¹Institute of Microstructure Technology, Karlsruhe Institute of Technology, Hermann-von-Helmholtz-Platz 1, 76344 Eggenstein-Leopoldshafen, Germany; ²Institute of Functional Interfaces, Karlsruhe Institute of Technology, Hermann-von-Helmholtz-Platz 1, 76344 Eggenstein-Leopoldshafen, Germany and ³Institute of Nuclear Physics, Ibragimova St. 1, 050032 Almaty, Kazakhstan

Correspondence: Swati Sharma (swati.sharma@kit.edu)

Received: 3 August 2018 Accepted: 19 December 2018

Published online: 10 January 2019

that can be used as guidelines for preparing application-specific laser carbon.

In this contribution we report on (i) an extensive characterization of Kapton-derived laser carbon produced in air and nitrogen environments with variable IR laser parameters, and (ii) fabrication of a flexible, pH-based enzymatic urea sensor using laser carbon, for demonstration purposes. Urea measurement is most commonly associated with the medical diagnosis of kidney dysfunction.²³ Current methods for urea determination in the urinary metabolites are unsuitable for integration with point-of-care testing platforms, such as catheters²⁴ that would allow for a rapid and contamination-free analysis. Increased urea levels can also cause a variety of other health hazards including cardiovascular events,²⁵ incident diabetes mellitus²⁶ and cognitive impairment,²⁷ and therefore entail monitoring in the food items,²⁸ and in the soil.²⁹ A widespread urea analysis method utilizes the enzyme urease, which catalyses the hydrolysis of urea into carbon dioxide and ammonia.³⁰ This ammonia is in turn detected using analytical platforms such as transducers,^{30–32} or by a direct pH-change measurement.

Various carbon materials, such as screen-printed carbon inks,³³ modified glassy carbon electrodes,^{34,35} carbon paste electrodes,³⁰ and carbon nanotubes (CNTs)³⁰ and their mixtures with materials, such as gold nanotubes³⁶ have been investigated for electrochemical urea sensor fabrication. Among these, the CNT and gold nanotube sensor³⁶ is a flexible device proposed for its application as a skin patch to determine urea levels in human sweat. While some of these devices are capable of detecting μM urea concentrations, they are fabricated employing cumbersome techniques and relatively expensive materials. To our knowledge, there is no report on a catheter-compatible, disposable urea sensor based on low-cost carbon materials.

There are two major challenges in the fabrication of urease-based urea sensor: (i) the chemisorption of urease onto a substrate typically leads to a drastic decrease in its activity,³⁷ and (ii) the shortening of the useful life-time of urease.^{30,32} To overcome these problems, the enzyme can be immobilized onto a substrate that mimics its natural environment, for example, chitosan.³⁷ The hydroxyl and amino groups present in chitosan enable both electrostatic and covalent immobilization strategies, and hence, increase the quantity of the immobilized enzyme. Chitosan films can be prepared on various conductive substrates via electrodeposition.^{38–40} We demonstrate urease immobilization both with and without the electrodeposited chitosan layer onto laser carbon substrates.

RESULTS

Fabrication and investigation of carbonization mechanism

The experimental strategy is schematically represented in Fig. 1, followed by a detailed description of the individual steps. Laser pyrolysis under nitrogen flow was carried out inside a poly(methyl methacrylate) (PMMA) chamber (50 mm \times 50 mm \times 12 mm) with a barium fluoride (BaF_2) window on the top (digital image in Fig. S11). One millimeter-thick BaF_2 has >90% transparency in the selected wavelength. The carbonization threshold (minimum value for obtaining a uniform carbon film) was found to be at a fluence (optical energy density of the laser beam) of 1.3 J cm^{-2} , below which the Kapton displayed bleaching. Fourier transform infrared (FTIR) spectroscopy was carried out to investigate the chemical nature and the absorbance of the bleached and residual Kapton films, pre-carbonization, and post-carbonization. The absorbance for the virgin (untreated) Kapton, and Kapton films after exposure to laser radiation (wavelength: $10.6 \mu\text{m}$) at fluences

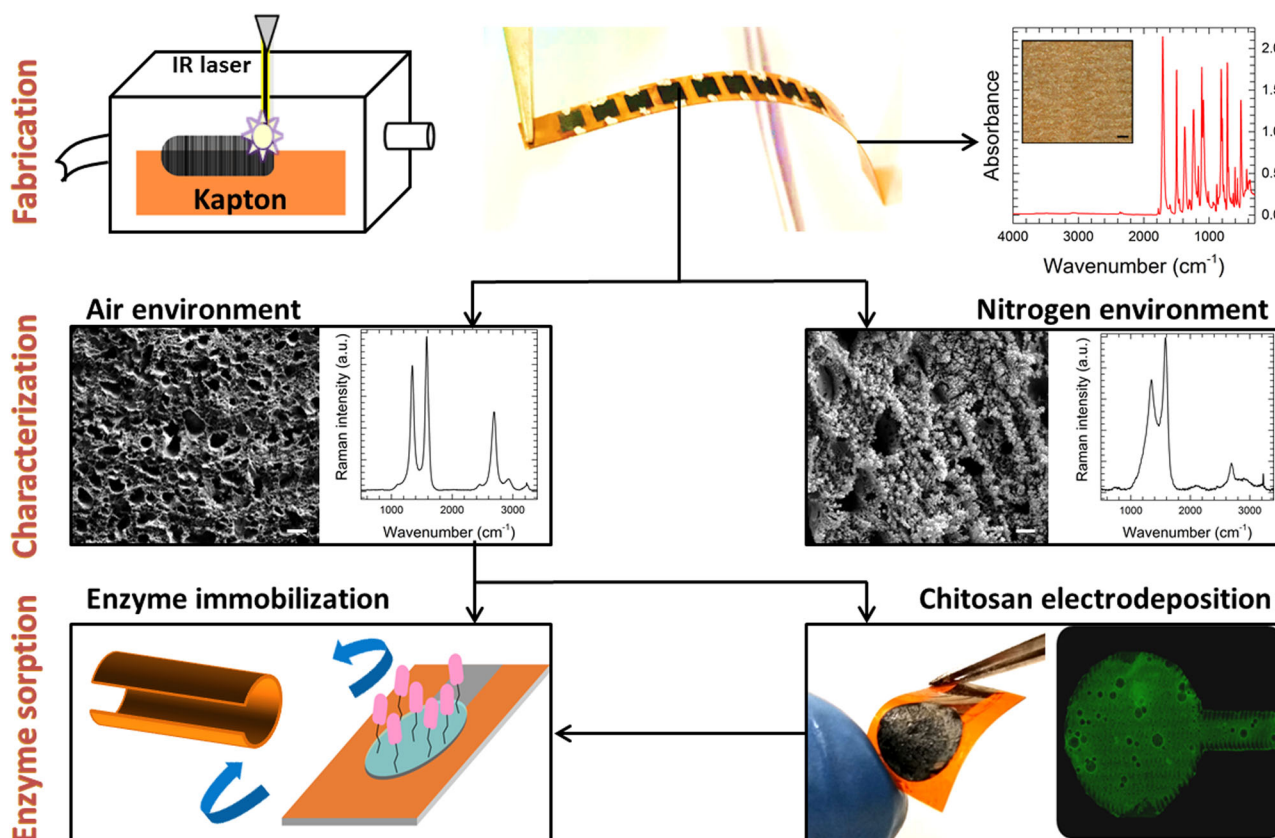


Fig. 1 Schematic diagram of the experimental approach. Process steps: fabrication of carbon structures on Kapton, characterization of laser carbon, and enzyme adsorption on laser carbon with and without chitosan layer. Scale bars on the SEM micrographs are $10 \mu\text{m}$. Parts of this image are adapted from Mamleyev et al.⁵⁸

1.1 and 1.2 J cm⁻² were 0.09, 0.19, and 0.12, respectively. The post-carbonization residual Kapton exhibited an absorbance of 0.15, which was higher compared to the untreated film. In the case of 1.2 J cm⁻² fluence, occasional carbon islands could be observed in the optical micrographs. One representative FTIR spectrum is shown in Fig. 1 (top right), and detailed absorbance profiles with the corresponding optical micrographs are provided in the Supplementary Information (Fig. S12).

Digital photograph and corresponding scanning electron microscope (SEM) images of a representative flexible carbon pattern showing three different regions: (i) bleached Kapton, and laser carbon prepared in (ii) air, and (iii) under nitrogen flow, are shown in Fig. 2a–e. The bleached areas contain bubbles (Fig. 2c) of an average diameter of ~30 μm. Evidently, laser carbons prepared in air (Fig. 2d) and nitrogen (Fig. 2e) display different porosity, which was further investigated using the argon isotherms, based on the Brunauer–Emmett–Teller (BET) theory.

Characterization and laser parameter optimization

Several batches of carbon patterns were fabricated employing various fluences in the 1.8–4.5 J cm⁻² range, with a 0.5 J cm⁻² increment. We observed that above 3.5 J cm⁻² fluence, the carbon films start to peel-off, and thus the resulting patterns are not useable for device fabrication. Therefore, three fluence values, 1.8, 2.3, and 3.5 J cm⁻² were chosen for further experiments, where the laser power and speed were varied. Samples were prepared in air and under nitrogen flow for each parameter set. First

evaluations were based on the morphology of the carbon film (uniformity, delamination), surface porosity, graphitic content, electrical conductivity, and fabrication reproducibility. SEM images of a typical delaminated film are provided in the Supplementary Information (see Fig. S13). Five samples (each prepared in air and nitrogen) that exhibited relatively high graphitic contents and electrical conductivity values were selected for further analysis. The carbon film thickness, Raman ratio (I_D/I_G) and electrical conductivity of these samples are listed in the Table 1. As it can be observed, the films prepared in air are ~50 μm thick, while those under nitrogen flow are ~30 μm. The I_D/I_G value, which indicates the ratio of the disordered to crystalline fraction in the carbon, is the lowest for samples A1 and N1, among the air and nitrogen prepared samples, respectively. SEM micrographs and surface porosity data for all fabricated samples are provided in the Supplementary Information (see Fig. S14, S15 and Table S11).

Figure 3 presents high-resolution X-ray photoelectron spectroscopy (XPS) data for C 1s, N 1s and O 1s. In all cases, the C 1s line was centered, and seven carbon containing species were found at the following binding energies: C = C at (284.2 ± 0.2) eV, C–C/C–H at (284.9 ± 0.1) eV, C–N at (285.7 ± 0.1) eV, C–O at (286.4 ± 0.2) eV, C = O at (287.2 ± 0.1) eV, O–C = O at (288.7 ± 0.1) eV, and a shake-up arising from aromatic rings at (290 ± 0.8) eV. Five nitrogen-based species were determined from the N 1s line, namely: pyridinic (N6) (398.5 ± 0.3) eV, amide (399.6 ± 0.2) eV, pyrrolic (N5) (400.1 ± 0.1) eV, quaternary (NQ) (401.7 ± 0.2) eV, and oxidic (NX) (404.2 ± 0.2) eV.^{41–44} From the O 1s spectra, five oxygen containing

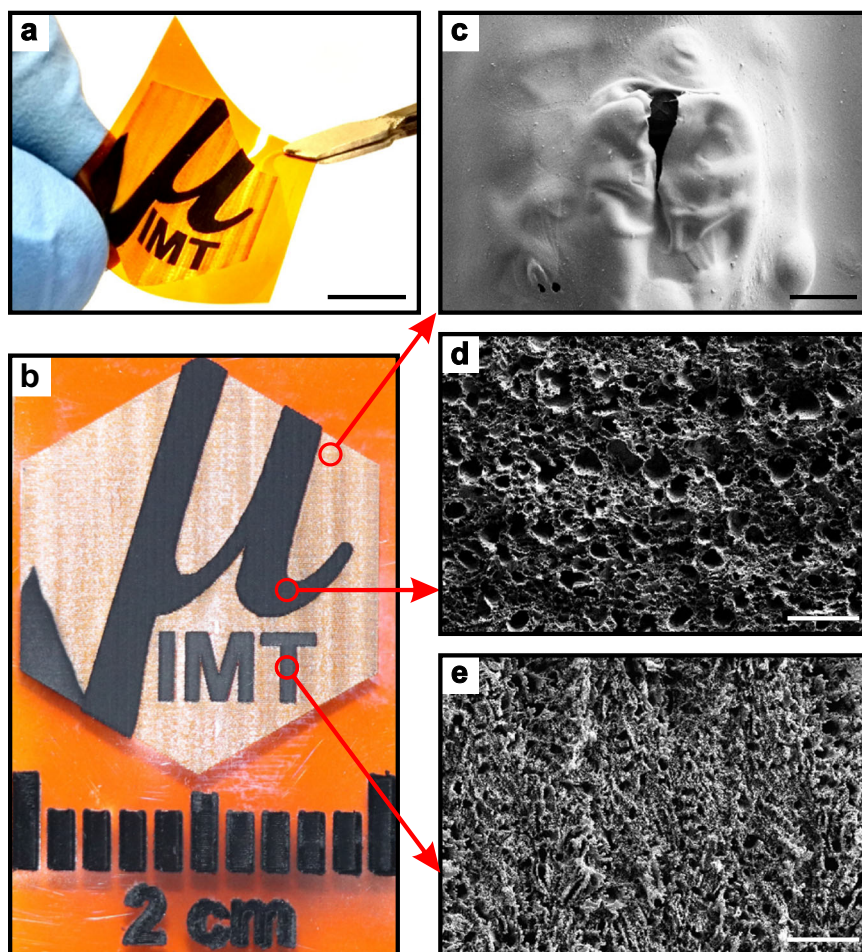


Fig. 2 **a** Photograph of a bendable laser carbon test structure on Kapton (scale bar: 1 cm). **b** Optical micrograph of a laser carbon sample showing three different regions. SEM micrographs of: **(c)** bleached Kapton surface at fluence below carbonization threshold; and carbon surface produced by laser radiation **(d)** in air and **(e)** in nitrogen environment. Scale bar in **c**: 15 μm; **d** and **e**: 50 μm

Table 1. Comparison of laser carbon samples prepared in air and nitrogen at variable fluence and power

Sample name	Fluence (J cm^{-2})	Power (W)	Carbon film thickness (μm)	Raman ratio $\frac{I_D}{I_G}$	Electrical conductivity (S cm^{-1})
<i>Fabricated in air</i>					
A1	1.8	4.8	48.5 ± 3.4	0.8	7.1 ± 0.7
A2	2.3	2.8	45.1 ± 3.8	1.0	5.1 ± 0.3
A3	2.3	4.8	55.3 ± 4.1	0.9	6.4 ± 1.1
A4	3.5	2.8	48.0 ± 7.0	1.6	6.9 ± 0.9
A5	3.5	4.8	48.9 ± 4.5	1.2	8.1 ± 2.0
<i>Fabricated in nitrogen</i>					
N1	1.8	4.8	25.0 ± 1.7	1.1	23.4 ± 2.3
N2	2.3	2.8	23.4 ± 1.9	1.4	12.0 ± 1.6
N3	2.3	4.8	35.4 ± 4.7	1.4	9.9 ± 1.4
N4	3.5	2.8	42.5 ± 1.6	1.4	9.0 ± 0.8
N5	3.5	4.8	65.2 ± 3.1	1.4	7.8 ± 0.6

species were detected: the aliphatic and aromatic carbonyl species (C=O) at (530.7 ± 0.1) and (532.1 ± 0.1) eV, respectively, amide at (531.4 ± 0.1) eV, aromatic ether group (C–O–C) at (533.0 ± 0.1) eV and hydroxyl (C–OH) at (533.9 ± 0.2) eV. All spectra featured widening in hydroxyl line due to the contamination from undefined species in the environment. There was a measurable increase in the C 1s and N 1s, and a decrease in the O 1s content with the corresponding functional groups in the nitrogen prepared samples. A widening of each species suggesting an increased disorder on the surface was observed for all samples prepared in nitrogen along with an increased asymmetry in the N 1s component. This can be attributed to the contribution from the quaternary species due to the interference of nitrogen. In the specimens A3 and N3, a narrowing of the full width at half maximum (FWHM) for C=C, C–N, C–O, and C=O peaks in the C 1s spectra were observed, which indicates that these specific laser parameters favor a higher carbon content on the surface, irrespective of the gaseous environment. The survey spectra, integrated peak areas, and the XPS data on thermally pyrolyzed Kapton are provided in the Supplementary Information (see Fig. S16, Table S12, and Fig. S17c–f).

Figure 4a, b are the collections of Raman spectra for the five selected samples, fabricated in air and nitrogen. In all cases, two distinctive first-order peaks at $\sim 1340 \text{ cm}^{-1}$ (D-band; A_{1g} breathing mode of the hexagonal rings at the K-point initiated by disorder), and $\sim 1580 \text{ cm}^{-1}$ (G-band; E_{2g} mode at the Γ -point, responsible for the stretching vibrations in all sp^2 carbons),⁴⁵ as well as the second-order 2D overtone (characteristic of all sp^2 carbons) at $\sim 2690 \text{ cm}^{-1}$ were present. The FWHM for the samples prepared in air was $51 \pm 8 \text{ cm}^{-1}$ for the G-band, and $59 \pm 10 \text{ cm}^{-1}$ for the D-band (Fig. 4a). For the samples fabricated under nitrogen the FWHM of both peaks noticeably increased to 77 ± 5 and $149 \pm 17 \text{ cm}^{-1}$ (Fig. 4b). For air samples, an increase in the fluence rendered the G-band relatively asymmetric. The 2D band noticeably decreased and widened in the nitrogen environment. The additional spectral lines at ~ 2460 , ~ 2930 , and $\sim 3230 \text{ cm}^{-1}$ are designated as (T+D) and (D+G), respectively. These Raman bands are generally present in polymer-derived carbons such as glassy carbon.⁴⁶

Two samples, namely, A1 and N1 were selected for further analysis due to their highest graphitic content. These two samples were also employed in urea sensor fabrication, and their properties were compared with that of a thermally carbonized Kapton

film. A direct comparison of their physicochemical properties are listed in Table 2. Detailed analyses based on the individual characterization methods are described below.

Figure 4c depicts the XRD patterns for virgin Kapton, a Kapton film pyrolyzed at 900°C , and the powders extracted from samples A1 and N1. The (002) peak, indicative of the graphite basal planes, was present in pyrolyzed Kapton, A1 and N1 at 2θ 25.7° , 25.6° , and 25.9° , respectively. The peak present in the virgin Kapton at 26.1° is a result of the stacked aromatic sheets characteristic of the polymer. The highest intensity peak of the Kapton 21.8° is completely absent in all types of carbon. The other characteristic graphite peak that corresponds to the (100) plane was present at 42.9° for pyrolyzed Kapton, and at 42.6° in both A1 and N1. Among carbon samples, the peaks featured the highest FWHM for the sample A1. The interlayer distance (d -spacing), calculated using Bragg's diffraction law, was 3.48 and 3.44 Å for A1 and N1, respectively. All calculated values are listed in Table 2. The Gaussian peak in the 2θ range 10 – 20° can potentially result from the residual Kapton impurities (as evidenced by the diffractogram of virgin Kapton) and disorder. Other peaks that are commonly present in graphitic carbons (considering the spacegroup $P6_3/mmc$) are (102) at 50.6° , reflection (004) at 53.2° , (104) at 70.5° , and (110) at 78.3° are also indicated.

Argon isotherms of A1 and N1 revealed a specific surface area of 255 and $106 \text{ m}^2 \text{ g}^{-1}$, respectively (Table 2), with maximum pore fraction in the 1.2–1.3 nm range in both materials. Further details on pore size distribution are provided in the Supplementary Information (see Fig. S18). According to the elemental analysis A1 and N1 contain $\sim 93\%$ and $\sim 97\%$ carbon (details in Table 2). Thermally carbonized Kapton exhibits a much lower carbon content.

In order to determine if the porosity distribution is same throughout the depth of the films, SEM images and Raman spectra were collected from the cross-sections of A1 and N1, as shown Fig. 4d, e and g, h. As it can be observed in the SEM images, the porosity at the film surface is significantly different from the center of the film. As one goes closer to the Kapton surface, the pore distribution changes. Raman spectra confirmed that the two sample types have one common feature: closer to the bottom of the film, the intensity of both, the G-band and 2D-band decrease. The 2D-band is not detectable in the bottom $\sim 10 \mu\text{m}$. Additionally for both specimens a sharp peak at $\sim 3230 \text{ cm}^{-1}$ was observed corresponding to amine stretching.⁴⁷

TEM micrographs of A1 and N1 are shown in Fig. 4f, i. The powder diffraction patterns indicate the absence of a long-range order, which is typical of polymer-derived carbons and is also substantiated by the XRD analysis. The diffusion rings (shown as insets) have minor shape variations. N1 features a relatively more graphitic structure (higher L_c according to XRD). In the case of A1, no thick stack of (turbostratic) graphenic fragments (L_c) could be detected despite an extensive search. Occasional evidences of a slightly higher L_c could be observed for N1. The images from these specific regions are provided in the Supplementary Information (Fig. S19).

Urea sensor fabrication and analysis

For urea sensor fabrication, a relatively large structure (circle of 8 mm diameter, shown in Fig. 1) was chosen. Two types of enzyme immobilization schemes were tested: (i) directly onto the carbon surface, (ii) via an intermediate electrodeposited hydrogel, chitosan. For the bare carbon film, urease immobilization was conducted in four different ways: (i) as-fabricated film, (ii) as-fabricated film with glutaraldehyde linker, (iii) oxygen plasma-treated film, and (iv) oxygen plasma-treated film with glutaraldehyde linker. Measured pH values with respect to time for these four cases are shown in Fig. 5a. A similar circular pattern, connected to a silver contact pad, was used as the electrode for

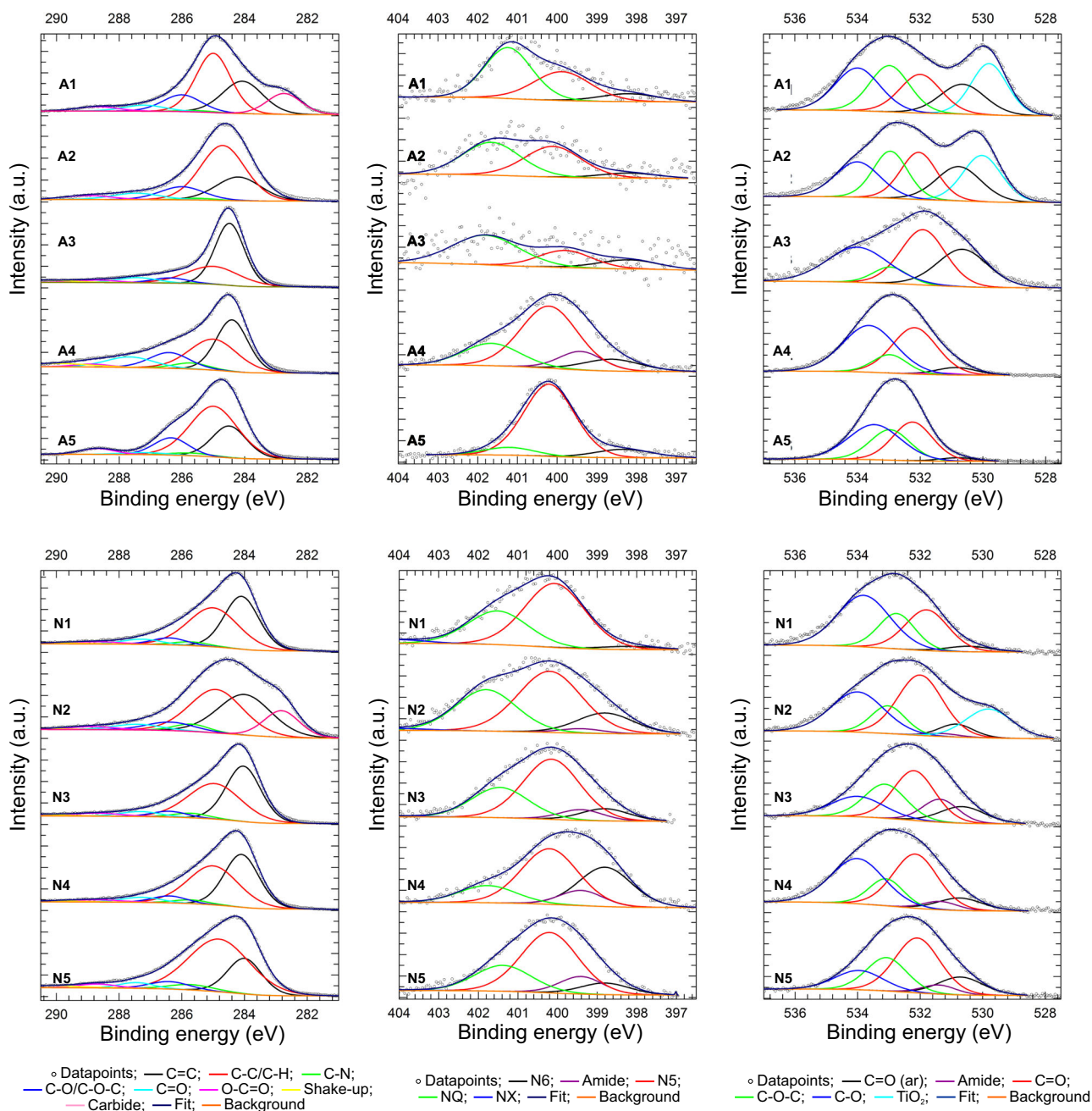


Fig. 3 Deconvoluted XPS spectra of C 1s, N 1s, and O 1s lines of laser-induced carbon fabricated in (top) air and (bottom) nitrogen

chitosan electrodeposition (photograph and fluorescence microscopy image shown in Fig. 1). Urease was immobilized via glutaraldehyde coupling to the deposited chitosan, and the sensitivity to urea using this assembly is depicted in Fig. 5b. The initial urease concentration was 1 mg/ml. As can be observed, within the 10^{-4} – 10^{-1} M concentration range, the rate of urease catalysis increases with the increase in the urea concentration.

In Fig. 5c, the two immobilization schemes along with the control experiments (carbon and chitosan surfaces without urease), are compared with urease activity in solution. Here, the urea concentration was maintained constant (10^{-2} M), and for the solution experiments urease concentration was varied in order to estimate the fraction of active urease on different sensor types.

In Fig. 5d we show a comparison of the urea sensing capabilities of a rolled-up and a flat urea sensor of the same surface area. Evidently, the sensor performance is almost identical in both

cases. A similar structure was rolled-up and fixed inside a tube, and a pH indicator paper was inserted in the forward flow direction. A 10^{-2} M urea solution was passed through this assembly, which turned the yellow/green pH paper into pink/purple color (residence time: 50 s), confirming a basic pH caused by the hydrolysis of urea. A video of this process can be found in the online Supplementary Information (Video SI V1).

DISCUSSION

Laser-induced carbonization entails a thermochemical decomposition of Kapton, similar to the pyrolysis performed in a furnace. However, since the process is much faster, the cleavage of chemical bonds is much more rapid, which renders the resulting material significantly different from both glassy and activated carbon. Kapton is a product of the condensation of pyromellitic

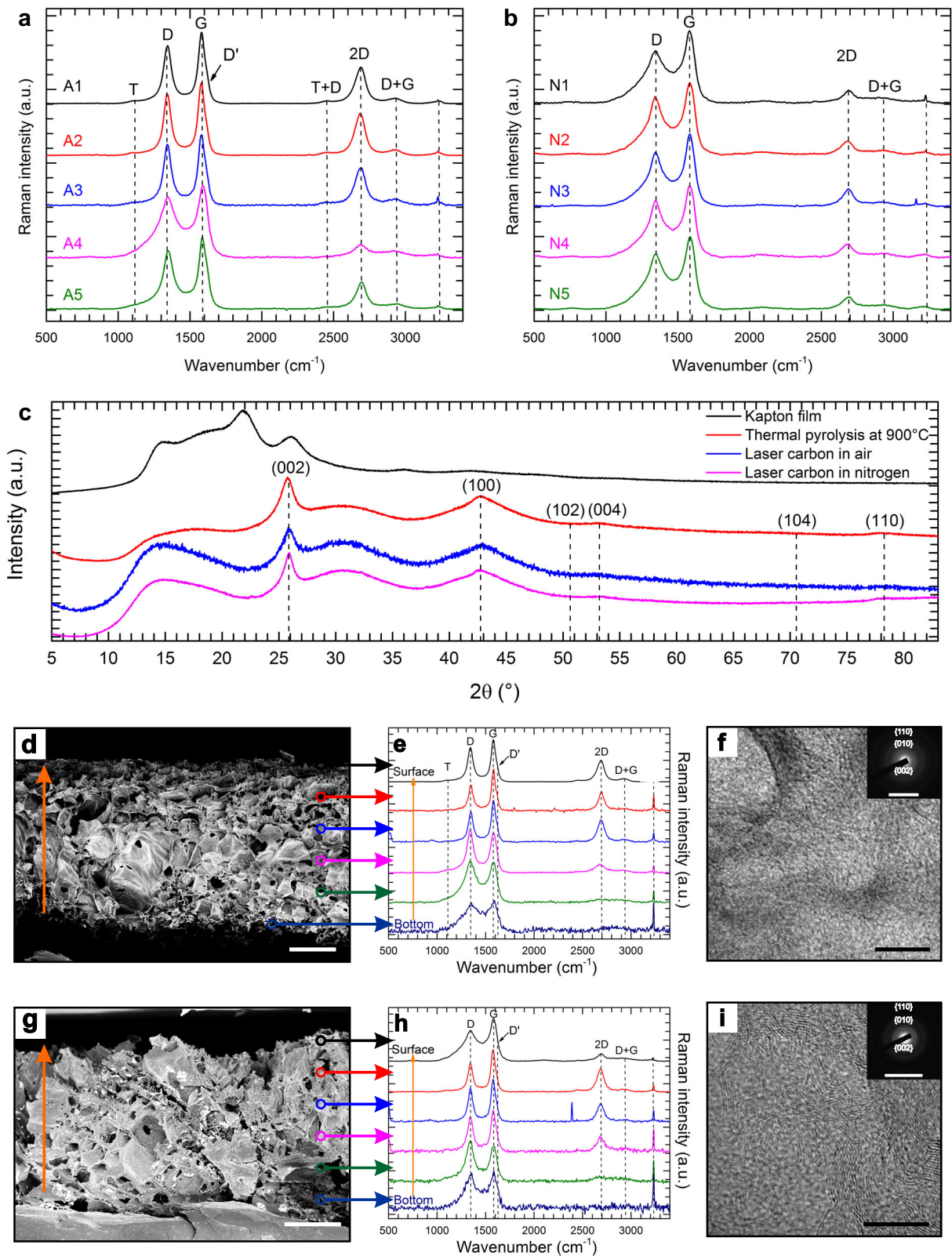


Fig. 4 Comparative Raman spectra of five selected laser carbon samples fabricated in (a) air and (b) under nitrogen flow. (c) X-ray diffractograms collected from virgin Kapton, Kapton pyrolyzed at 900°C and two selected laser carbon powder samples A1 and N1. **d–f** Cross-sectional SEM images, Raman spectra recorded at every $\sim 8\ \mu\text{m}$ distance along the cross-section, and TEM images with the selected area diffraction pattern shown in the respective insets for A1 and (g–i) N1. Arrows (from **d** to **e** and from **g** to **h**) show the locations of the collection of Raman spectra. Scale bars in (d, g): $10\ \mu\text{m}$; (f, i): $10\ \text{nm}$; insets of (f, i): $10\ \text{nm}^{-1}$

dianhydride and 4,4'-oxydiphenylamine (PMDA/ODA), that features an optical transparency of 79% in the mid-IR wavelength. According to the Beer–Lambert law, the laser intensity decreases with the propagation of the beam within the sample volume. The energy of a single photon in the mid-IR wavelength is ~ 0.12 eV, which is insufficient for a direct bond dissociation of the polymer molecules. Consequently, the radiation induces phonons in Kapton. This vibrational energy is released by a bond dissociation

	Air	Nitrogen	Thermal pyrolysis at 900 °C
Elemental analysis, %			
C	93.1 ± 0.3	95.7 ± 1.4	81.7 ± 2.0
N	0.9 ± 0.1	1.0 ± 0.1	6.0 ± 0.2
H	0.4 ± 0.02	0.5 ± 0.2	0.9 ± 0.2
XPS, %			
C 1s	76.0	92.0	93.5
N 1s	1.0	2.5	1.6
O 1s	23.0	5.5	4.9
Crystallite size, L_a (XRD) (nm)	4.0	3.6	3.6
Crystallite size, L_c (XRD) (nm)	7.1	8.6	5.1
Interlayer distance (Å)	3.48	3.44	3.47
Conductivity ($S\ cm^{-1}$)	10.2 ± 2.4	23.4 ± 2.3	100 ⁶⁰
Contact angle	70	120	75
BET surface area ($m^2\ g^{-1}$)	255	106	–

in the weaker pyridine component of the PMDA followed by material ablation from the surface (similar to etching),^{13,48,49} and is expressed as bleaching when the fluence is below the carbonization threshold ($1.3\ J\ cm^{-2}$). The ablated material is released in the form of bubbles (Fig. 2c) that cause the Kapton to swell roughly by $\sim 5\ \mu m$. This bubble-containing film now features a reduced absorbance, 0.19. In the case of a higher fluence (still lower than the carbonization threshold), the absorbance is between that of the virgin Kapton and a lower fluence due to the presence of more bubbles.

Further increase in the fluence leads to an immediate burst of such bubbles, resulting in a rapid release of the volatile products, which primarily constitute CO_2 , CO , HCN , C_6H_6 and radicals resulting from Kapton fragmentation.⁷ Under constant radiation, this mixture becomes ionized and forms a plume (plasma-like glow discharge⁵⁰). The plume-shield prevents further beam penetration in the film, causing heat generation at the beam-front and adjacent areas.⁵⁰ We propose that this heat, in turn, carbonizes the film. This is substantiated by the fact that the carbonization only occurs when the plume is formed (can be observed as a bright spot through the naked eye; see video SI V2 in the Supplementary Information). A fast release of pyrolysis byproducts generates pores in the material, distributed over several microns below and a few microns above the Kapton surface. The remaining Kapton film underneath the carbon layer displays a lower absorbance, 0.15. Importantly, all FTIR spectra resemble the same profile as the virgin polymer, with variations in the individual peak intensities. This implies that the chemical composition of the uncarbonized Kapton is preserved throughout; only the fraction of different surface functional groups changes.

In most reports on laser carbon, the material is obtained in air (ambient conditions), while a few studies utilize an inert

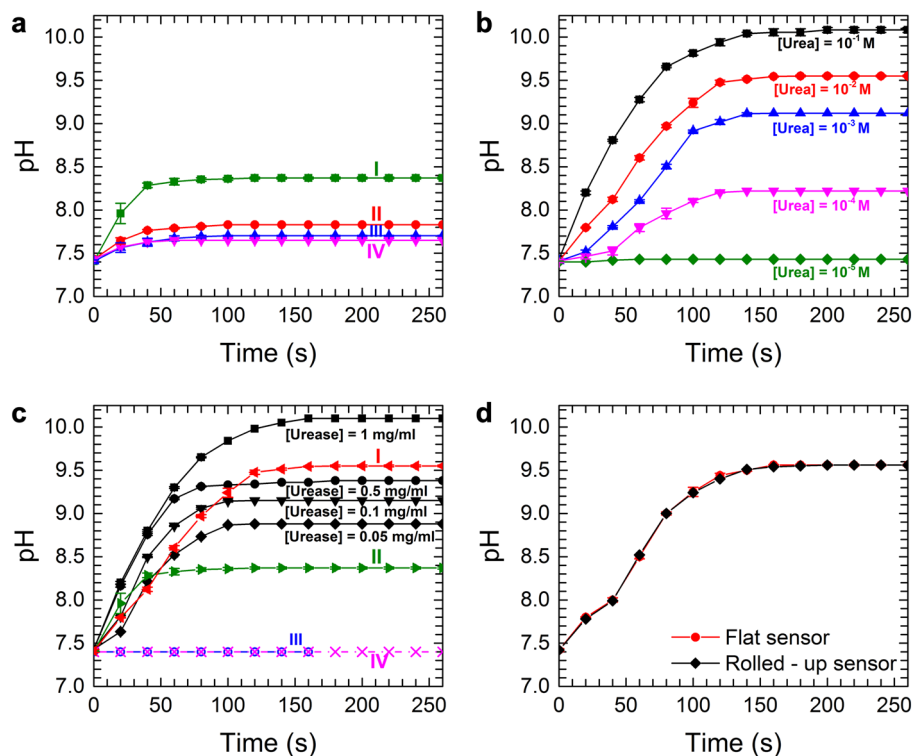


Fig. 5 **a** Urease activity on (I) the untreated carbon film, (II) coupled to glutaraldehyde; [urea] = 10^{-2} M in all cases. **b** Urea detection using chitosan–urease sensors. The film was exposed to a 1 mg/ml urease solution for immobilization and thoroughly washed before exposure to the urea solutions. **c** Urease activity in solution (black curves), and (I) the sensor with electrodeposited chitosan and (II) in the presence of the untreated film; (III, IV) control film, untreated with and without electrodeposited chitosan, respectively. Urea concentration is 10^{-2} M in all cases. **d** Urease activity of flat and rolled-up sensors; [urea] = 10^{-2} M. All measurements were performed in triplicate, and data points report the mean \pm standard deviation

environment.^{51,52} During our initial experiments, we observed that the laser carbon fabricated under nitrogen was hydrophobic (contact angle $\sim 120^\circ$), while the air-fabricated carbon was hydrophilic (contact angle: $\sim 70^\circ$). This is unsurprising, as the carbons prepared in the presence of oxygen often carry oxygenated surface functional groups. Nitrogen, on the other hand, facilitates inert surroundings and limits the formation of such groups. According to the surface functionality analysis based on XPS, the nitrogen-prepared sample exhibits a higher fraction of surface carbon compared to that prepared in air, which is in line with the elemental analyses (Table 2). However, the exact elemental compositions analyzed by these two techniques do not match, as the elemental analysis is performed on bulk powder, while XPS data is from the top ~ 10 nm of the film. Among the detected functional groups, the polar ones such as hydroxyl ($-\text{C}-\text{OH}$), aliphatic and aromatic carbonyl ($-\text{C}=\text{O}$), and with nitrogen heteroatom ($-\text{CN}$) are associated with hydrophilicity, while $\text{C}=\text{C}/\text{C}-\text{C}-\text{H}$ species render the material hydrophobic. The deconvoluted high-resolution spectra shown in Fig. 3 indicate that in all air-prepared samples, the fraction of polar groups (carbonyl and carboxyl) is higher, and in the nitrogen samples, the non-polar groups ($\text{C}=\text{C}/\text{C}-\text{C}-\text{H}$) are more abundant. Cyano group ($-\text{C}\equiv\text{N}$) is present in both samples; however, its fraction is very low ($<3.5\%$ in air and $<5\%$ in nitrogen, also see Fig. 3 and Table S12), which does not seem to have a strong influence on the hydrophilicity. Additionally, in all nitrogen samples, the nitrogen content, in particular the quaternary nitrogen, is higher. An important observation from the XPS data is the widening of all peaks for nitrogen prepared samples compared to those in air confirming an higher degree of disorder.

Raman spectra for air fabricated samples exhibited sharp D and G-bands, with the best separation in the case of the lowest fluence (sample A1). The general trend is that both G and D bands widen with an increase in the fluence, and a higher laser power improves the band separation. For example, samples A4 and A5 are prepared at the same fluence but A5 with a higher power. Sample A1 also featured the strongest 2D-band, which signifies that among the air-fabricated samples, this material has the highest graphitic content (also see Table 1). The same parameter set yielded the highest graphitic content for the nitrogen prepared sample (i.e., N1). Generally, air-fabricated samples show a better peak separation, as well as an increasing 2D peak intensity with the changing laser parameters, while this effect is not so obvious in the case of nitrogen prepared samples. This indicates that the graphitic content is not strongly affected by the laser parameters when the material is prepared in an inert environment. Based on the Raman data, it can be deduced that the nitrogen prepared samples feature a higher surface disorder, which is in line with the XPS data, however, contradicts the information obtained from the electrical conductivity, TEM and XRD. This can be explained by the differences in surface and bulk properties of the material. Both XPS and Raman are measured on the sample surface (10 nm and <1 μm deep, respectively), while other measurements are performed on bulk.

It is well-known that polymer-derived carbons contain a significant number of in-plane defects.^{5,53} Although the physical properties of laser carbon are different from glassy carbon, it is reasonable to assume that the material features a high fraction of defects, as well as some impurities that are evident from the elemental analysis. Both the defects and heteroatoms result in a turbostratic structure (misaligned basal planes), which causes the graphenic fragments to fold.⁵ Consequently, there is a lot of strain within the crystallites, and the C-C bond-lengths, as well as the valence angles are distributed over a range.⁵³ This causes the (100) peak to broaden (Fig. 4c). If the exact strain contribution is identified and subtracted, the crystallite size calculations can be more accurate. However, with the available microstructural data strain contributions cannot be quantified, hence we assumed the

$P6_3/mmc$ spacegroup for the XRD calculations. It is clear from a direct comparison of all diffractograms in Fig. 4c that the Kapton is almost completely degraded after its laser carbonization.

The microstructural differences in surface and bulk were confirmed by the cross-sectional SEM imaging and Raman spectroscopy. In the cross-sectional Raman, a small but sharp peak at $\sim 3230\text{ cm}^{-1}$ for amine ($-\text{NH}_2$) stretching is observed, which results from the residual Kapton impurity, and becomes more prominent along the depth of the film. From the cross-sectional SEM micrographs (Fig. 4f, i), one can clearly visualize a hierarchical porosity distribution in the air-fabricated sample. The nitrogen sample, on the other hand, features a more or less uniform porosity throughout. Its Raman data however, indicates that there is an increasing graphitic content from its base to the top, which is drastically different for the top $1\ \mu\text{m}$. The disordered carbon content, which was apparently higher for nitrogen samples during XPS and Raman measurements, but lower in XRD can be justified by a hierarchical material structure. The porosity observed in the SEM images (taken from the top) does not match with that determined by BET (Table 2) for the same reason. Importantly, the DFT model based on cylinder and sphere type pores was used for the porosity determination, which is limited to 50 nm pore size. The maximum number of pores were observed in the 1.2–1.3 nm range, and the overall pore volume was 0.37 and 0.28 $\text{cm}^3\text{ g}^{-1}$ in A1 and N1, respectively. Larger pores are visible in the SEM micrographs (surface and cross-sectional), and are analyzed using the imageJ software (details provided in the Supplementary Information Figs. S14, S15).

Laser carbon obtained in both air and nitrogen can potentially facilitate enzyme absorption. From XPS, the functional groups can be recognized but their activity towards various chemical species cannot be confirmed. Therefore, the mechanism of enzyme immobilization on the untreated carbon is not clear at this point. We observed that the use of glutaraldehyde indeed reduced the yield of catalytically active enzyme (Fig. 1). There could be three plausible explanations: (i) glutaraldehyde undergoes self-polymerization, or facilitates protein polymerization, and thus reduces the bound active urease fraction; (ii) glutaraldehyde reacts only with substrate active groups, removing both itself and potential substrate reactive sites from urease attachment; (iii) the non-specific glutaraldehyde reaction with urease renders some fraction of the enzyme catalytically inactive. In order to increase the active fraction of enzyme, one can utilize the second pathway of electrodepositing an intermediate chitosan layer on carbon. Chitosan, a biocompatible, biodegradable, and non-toxic biopolymer,⁵⁴ provides a hydrogel matrix that mimics the cellular microenvironment of urease, which is conducive for enzyme activity preservation. The resulting irreversible Schiff's base effectively removes the cross-linked glutaraldehyde from the reaction, reducing the urease coupling.

In conclusion, we have described a direct laser writing method employing inexpensive and often readily available, industrial IR-laser platforms that is capable of patterning two-dimensional porous carbon structures of any pre-defined geometry on Kapton films for flexible device fabrication. Based on the parameter optimization we suggest that (i) a low fluence and high power are favorable for obtaining an enhanced graphitic content in laser carbon, and (ii) carbon prepared in air is more suitable for biosensor fabrication, as it features reactive points for water-soluble chemical and biochemical species such as enzymes. Properties of laser carbon can generally be tuned to achieve the desirable balance of electrical and surface properties by selecting the right laser parameters and pyrolysis environment. The smallest feature size depends on the laser spot size, which is in turn determined by the applied wavelength as well as the machine optics. Although laser-induced carbonization significantly differs from the conventional thermal pyrolysis of polymers in terms of speed, execution, and the properties of the resulting

carbon, the carbonization mechanism is still primarily thermal, except the heat is generated by the plume. Laser carbon features micro, macro as well as meso pores, with a different top 1 μm layer from the rest of the material. This new addition to the pyrolytic carbon family is physically closer to carbons deposited from gaseous hydrocarbons, rather than to glassy carbon. However, its purity is much lower due to an extremely fast process, which is insufficient for a complete carbonization and experiences material redeposition.

We have demonstrated the fabrication of a pH-based, flexible, catheter-compatible urea sensor using laser carbon integrated with the underlying Kapton sheet, which can be readily used for in vivo urea determination. For biosensor fabrication, one can choose the type of laser carbon based on the desirable functional groups. We propose air prepared carbon for surface-based applications such as chemo- or biosensors, and nitrogen prepared sample for electronic applications due to its higher graphitic content. The ability to electrodeposit chitosan hydrogel films enables immobilization of a variety of enzymes (or bio-transducers) while maintaining biocompatibility. The reported device can successfully detect urea concentrations as low as (10^{-4} M), which is two orders of magnitude lower than the urea concentration in the blood serum of a healthy human, with a response time of less than one minute. The sensor can be conveniently rolled-up and fit inside a tube down to 3 mm internal diameter without any compromise in its performance. The materials and instruments required in the reported technique are low cost, which render it attractive to a large variety of potential users. In addition to biosensors, potential research areas that can immediately benefit include neural electrodes, energy storage devices, and pressure transducers.

METHODS

Fabrication

KaptonTMHN (DuPont; supplier: Krempel GmbH; thickness: 125 ± 13 μm) films were cleaned with acetone, isopropanol, and deionized water prior to laser irradiation on a ULS Versa Laser 3.50 set-up; with IR laser (wavelength: 10.6 μm), ~ 180 μm spot diameter; 1000 pulses/inch in raster mode with line spacing of ~ 100 μm . Fluence was calculated using the formula: $\Phi = \left(\frac{P_{\text{avg}} \cdot T}{\pi R^2}\right) \frac{1}{v}$, where P_{avg} is the applied average laser power, T is full period determined from PPI/v , where PPI is pulse/inch, v is speed of the focus carriage, and R is the spot radius. Fluence was adjusted by tuning the power and transit speed. Thermal pyrolysis was performed in a Carbolite Gero FHA 13 furnace at 900 $^{\circ}\text{C}$ for 1 h under 0.8 l min^{-1} nitrogen flow at a ramp rate of 5 $^{\circ}\text{C min}^{-1}$.

Characterization

FTIR was conducted on a Bruker Vertex 70 spectrometer in the 400–4000 cm^{-1} range, with ~ 2 cm^{-1} resolution. All absorbance coefficients were obtained for the wavenumber of the CO_2 laser, ~ 940 cm^{-1} , which corresponds to the out-of-plane bending of the C–H and C–H₂ functional groups.⁴⁷ Absorbance was corrected with Kubelka–Munk function and compared for all samples. SEM and TEM were carried out on Carl Zeiss AG—SUPRA 60VP SEM and JEOL-2100 TEM (200 kV using a nickel grid with carbon coating), respectively. Profilometry was carried out on a Dektak V 220-Si profilometer. Further details on sample preparation can be found in the Supplementary Information (Fig. S110). Sheet resistance of the films was determined by four probe van der Pauw method using copper contact pads on a 9-T Quantum Design Physical Property Measurement System (sourcemeater: Keithley 2460, nanovoltmeter: Keithley 2182A).

XPS was performed using Al-K α radiation ($E = 1486.6$ eV) and the spectra were collected with the hemispherical energy analyzer RG Scienta 4000. The survey and individual spectra were collected with 1 and 0.05 eV increments, respectively. Line correction was adjusted to C = C/C–C/C–H peak at 284.85 eV for all spectra, and according to the position of the corresponding peak in the thermally pyrolyzed specimen. In some spectra, additional Ti 2p peak was determined at ~ 458 eV due to the interference with the holder during measurements. This was utilized for the correction of peaks positions (see survey spectra in the Supplementary Information,

Fig. S16) during the analysis. Due to the Ti interference, additional peaks were observed in such samples in O 1s line corresponding to TiO_2 at 529.9 eV, and in C 1s—to carbide peak at 282.7 eV. These peaks were omitted in calculation of the global percentage, and the corresponding area was recalculated. All spectra were corrected using CasaXPS software with Shirley background and fitted with Voigt profile. For the peak assignment, the following fitting procedure was applied: (i) the best match was achieved in C 1s by assigning seven species, in the N 1s spectra with five species, and in O 1s with five species; (ii) the areas of the corresponding peaks were adjusted in different spectra, namely: the amide peak area from N 1s corrected into O 1s (only for nitrogen prepared samples); cumulative sum of N5, N6, and NQ from the N 1s spectra in C–N peak in C 1s; carbonyl, ether, and hydroxyl species from O 1s into suitable peaks in C 1s; (iii) after adjustment, the C=C and C–C/C–H lines were fitted, due to the variations in the contribution of additional phases.

Raman spectra were collected on a Bruker Senterra set-up (equipped with a confocal microscope), having spectral bandwidth of 70–3500 cm^{-1} with 5 cm^{-1} resolution using a DPSS laser ($\lambda = 532$ nm) at 2 mW power with a penetration depth of < 1 μm . An Olympus M-PLAN $\times 50$ NA 0.5 objective was used for observing the measured area and focusing the excitation-laser and collimation of the backscattered light, resulting in 2 μm spot. Peaks were fitted with a Voigt profile and integrated using OriginPro software. XRD was conducted on a Bruker D8 Advance diffractometer in θ – 2θ geometry using Cu-K $\alpha_{1,2}$ radiation. Crystallite size (L_c) and stacking thickness (L_s) were determined according to the Scherrer formula, based on the method described by Warren.⁵⁵ Elemental analysis was performed on ELEMENTAR Vario Micro cube. Porosity and specific surface area were determined measuring the argon adsorption isotherms at 87 K with a Quantachrome Autosorb-1 MP, applying the and BET theory.⁵⁶ Porosity data were fitted using the DFT⁵⁷ (Quantachrome software Autosorb 1.54).

Urea sensor

Details of urea sensor fabrication are reported elsewhere.⁵⁸ Briefly, urease from Jack Beans (*Canavalia ensiformis*, Sigma Aldrich) was immobilized onto carbon electrodes by immersing in a 1 mg ml^{-1} urease solution overnight,⁵⁹ with and without glutaraldehyde linker. The electrodes were treated with the oxygen plasma for 2 min, 100 W in one batch. Chitosan from crab shells (85% deacetylation, 200 kDa, Sigma Aldrich) was electrodeposited onto carbon electrodes, and urease was covalently coupled to chitosan via glutaraldehyde linker (25% in water, Sigma Aldrich). Five different solutions with a constant urea concentration (10^{-2} M) and variable urease content (0.05–1 mg/ml) were prepared, and their pH values were measured using (i) pH electrode (Mettler Toledo, InLab Routine Pro), and (ii) pH indicator paper for quantitative and qualitative measurements, respectively. A sensor (carbon–chitosan–urease assembly) was rolled-up and placed inside a Teflon tube of 3 mm internal diameter. A pH indicator paper was placed in the same tube at ~ 2 cm distance. The solution was held on top of the sensor for ~ 50 s, and then allowed to diffuse into the pH indicator paper (see Video SI V2 in Supplementary Information). For a comparison with the flat sensor, a similar structure was wrapped around a Teflon tube such that the enzyme containing surface is exposed to the urea solution.

DATA AVAILABILITY

Samples and detailed characterization data are available on request from S.S.

ACKNOWLEDGEMENTS

Authors sincerely thank Sandra Kauffmann-Weiss and Marco Langer from the Institute for Technical Physics, KIT for their help with the electrical conductivity measurements; Aakanksha Khurana and Akhilesh Sharma, Punjab Engineering College, Chandigarh, India (supported by PEBA at KIT), for help in laser fabrication and data analysis. E.M. and S.S. acknowledge funding by the Ministry of Science, Research and Arts, Baden-Württemberg, Germany (Az: 33-7533-30-20/3/3), HEIKA Center FunTECH-3D. N.N. and N.M. acknowledge funding from the Deutsche Forschungsgemeinschaft for the project Bio-PRICE (DFG MA 6653/1-1). N.N. wishes to thank the Ministry of Higher Education of Malaysia for the scholarship (SLAB Scheme) and the BioInterfaces International Graduate School (BIF-IGS, www.bif-igs.kit.edu). Authors acknowledge the support by Deutsche Forschungsgemeinschaft and Open Access Publishing Fund of KIT.

AUTHOR CONTRIBUTIONS

E.M. optimized and performed all laser carbonization experiments, contributed to FTIR and urea sensing experiments, and carried out primary data analysis. S.H. conducted Raman spectroscopy; A.N. conducted XPS; P.W. performed BET and XRD; and V.K. conducted TEM with respective data interpretation. N.N. carried out chitosan electrodeposition, enzyme immobilization, and urea detection tests, N.M. and K.L. provided the know-how on working with chitosan and urease enzyme, respectively. S.S. conceived the idea, designed the experiments, contributed to urea sensing experiments, and to the data analysis. E.M. and S.S. prepared the first draft of the manuscript. All authors contributed to manuscript preparation.

ADDITIONAL INFORMATION

Supplementary information accompanies the paper on the *npj Flexible Electronics* website (<https://doi.org/10.1038/s41528-018-0047-8>).

Competing interests: The authors declare no competing interests.

Publisher's note: Springer Nature remains neutral with regard to jurisdictional claims in published maps and institutional affiliations.

REFERENCES

- Sharma, S., Sharma, A., Cho, Y.-K. & Madou, M. Increased graphitization in electropun single suspended carbon nanowires integrated with carbon-mems and carbon-nems platforms. *ACS Appl. Mater. Interfaces* **4**, 34–39 (2012).
- Zakhradaeva, A. et al. Custom-designed glassy carbon tips for atomic force microscopy. *Micromachines* **8**, 285 (2017).
- Jenkins, G. M. & Kawamura, K. *Polymeric Carbon-carbon Fibre, Glass and Char*. (Cambridge University Press, Cambridge, 1976).
- Harris, Peter J. F. New perspectives on the structure of graphitic carbons. *Crit. Rev. Solid State Mater. Sci.* **30**, 235–253 (2005).
- Sharma, S., Kumar, C. N. S., Korvink, J. G. & Kübel, C. Evolution of glassy carbon microstructure: in situ transmission electron microscopy of the pyrolysis process. *Sci. Rep.* **8**, 16282 (2018).
- Sharma S. & Arpad M. et al. Micro and nano patternable magnetic carbon. *J. Appl. Phys.* **120**, 235107 (2016).
- Brannon, J. H., Lankard, J. R., Baise, A. I., Burns, F. & Kaufman, J. Excimer laser etching of polyimide. *J. Appl. Phys.* **58**, 2036–2043 (1985).
- Schumann, M., Sauerbrey, R. & Smayling, M. C. Permanent increase of the electrical conductivity of polymers induced by ultraviolet laser radiation. *Appl. Phys. Lett.* **58**, 428–430 (1991).
- Feurer, T., Sauerbrey, R., Smayling, M. C. & Story, B. J. Ultraviolet-laser-induced permanent electrical conductivity in polyimide. *Appl. Phys. A* **56**, 275–281 (1993).
- Phillips, H. M., Wahl, S. & Sauerbrey, R. Submicron electrically conducting wires produced in polyimide by ultraviolet laser irradiation. *Appl. Phys. Lett.* **62**, 2572–2574 (1993).
- Srinivasan, R., Hall, R. R., Allbee, D. C. & Hall, F. L. D. C. Generation of electrically conducting features in polyimide (Kapton) films with continuous wave, ultraviolet laser radiation. *Applied Physics Letters*, 3382,(Kapton T M) 3382, 1991–1993 (1993).
- Srinivasan, R., Hall, R. R., Wilson, W. D., Loehle, W. D. & Allbee, D. C. Formation of a porous, patternable, electrically conducting carbon network by the ultraviolet laser irradiation of the polyimide PMDA-ODA (Kapton). *Chem. Mater.* **6**, 888–889 (1994).
- Ortelli, E. E., Geiger, F., Lippert, T., Wei, J. & Wokaun, A. UV-laser-induced decomposition of Kapton studied by infrared spectroscopy. *Macromolecules* **33**, 5090–5097 (2000).
- Srinivasan, R. Ablation of polyimide (Kapton) films by pulsed (ns) ultraviolet and infrared (9.17 μm) lasers. *Appl. Phys. A* **56**, 417–423 (1993).
- Guo, X. D., Dai, Y., Gong, M., Qu, Y. G. & Helseth, L. E. Changes in wetting and contact charge transfer by femtosecond laser-ablation of polyimide. *Appl. Surf. Sci.* **349**, 952–956 (2015).
- In, J. B. et al. Facile fabrication of flexible all solid-state micro-supercapacitor by direct laser writing of porous carbon in polyimide. *Carbon N. Y.* **83**, 144–151 (2015).
- Nayak, P., Kurra, N., Xia, C. & Alshareef, Husam N. Highly efficient laser scribed graphene electrodes for on-chip electrochemical sensing applications. *Adv. Electron. Mater.* **2**, 1600185 (2016).
- Fenzl, C. et al. Laser-scribed graphene electrodes for aptamer-based biosensing. *ACS Sens.* **2**, 616–620 (2017).
- Xu, G., Jarjes, Z. A., Desprez, V., Kilmartin, P. A. & T.-S., Jadranka Sensitive, selective, disposable electrochemical dopamine sensor based on PEDOT-modified laser scribed graphene. *Biosens. Bioelectron.* **107**, 184–191 (2018).
- Lin, J. et al. Laser-induced porous graphene films from commercial polymers. *Nat. Commun.* **5**, 5714 (2014).
- Tao, L. Q. et al. An intelligent artificial throat with sound-sensing ability based on laser-induced graphene. *Nat. Commun.* **8**, 1–8 (2017).
- Zhang, J. et al. Efficient water-splitting electrodes based on laser-induced graphene. *ACS Appl. Mater. Interfaces* **9**, 26840–26847 (2017).
- Rysz, J., Gluba-Brzózka, A., Franczyk, B., Jablonowski, Z. & Cialkowska-Rysz, A. Novel biomarkers in the diagnosis of chronic kidney disease and the prediction of its outcome. *Int. J. Mol. Sci.* **18**, 1702 (2017).
- Choi, C. J., Wu, H.-Y., George, S., Weyhenmeyer, J. & Cunningham, B.T. Biochemical sensor tubing for point-of-care monitoring of intravenous drugs and metabolites. *Lab Chip* **12**, 574–581 (2012).
- Jujo, K. et al. Persistent high blood urea nitrogen level is associated with increased risk of cardiovascular events in patients with acute heart failure. *ESC Heart Fail.* **4**, 545–553 (2017).
- Xie, Y. et al. Higher blood urea nitrogen is associated with increased risk of incident diabetes mellitus. *Kidney Int.* **93**, 741–752 (2018).
- Kurella, M., Chertow, G. M., Luan, J. & Yaffe, K. Cognitive impairment in chronic kidney disease. *J. Am. Geriatr. Soc.* **52**, 1863–1869 (2004).
- Weber, J. V. & Sharypov, V. I. Ethyl carbamate in foods and beverages: a review. *Environ. Chem. Lett.* **7**, 233–247 (2009).
- Naz, M. Y. & Sulaiman, S. A. Slow release coating remedy for nitrogen loss from conventional urea: a review. *J. Control. Rel.* **225**, 109–120 (2016).
- Dhawan, G., Sumana, G. & Malhotra, B. D. Recent developments in urea biosensors. *Biochem. Eng. J.* **44**, 42–52 (2009).
- Hubalek, J. et al. Spectrometric and voltammetric analysis of urease—nickel nanoelectrode as an electrochemical sensor. *Sensors* **7**, 1238–1255 (2007). sensors-07-01238[PII].
- Singh, M., Verma, N., Garg, A. & Redhu, N. Urea biosensors. *Sens. Actuators B* **134**, 345–351 (2008).
- Ho, W. O. et al. Electrochemical sensor for measurement of urea and creatinine in serum based on ac impedance measurement of enzyme-catalyzed polymer transformation. *Anal. Chem.* **71**, 1940–1946 (1999).
- Kumar, T. H. V. & Sundramoorthy, A. K. Non-enzymatic electrochemical detection of urea on silver nanoparticles anchored nitrogen-doped single-walled carbon nanotube modified electrode. *J. Electrochem. Soc.* **165**, B3006–B3016 (2018).
- Rafiq, K. et al. Fabrication of a highly effective electrochemical urea sensing platform based on urease-immobilized silk fibroin scaffold and aminated glassy carbon electrode. *Sens. Actuators B* **251**, 472–480 (2017).
- Liu, Y.-L. et al. Flexible electrochemical urea sensor based on surface molecularly imprinted nanotubes for detection of human sweat. *Anal. Chem.* **90**, 13081–13087 (2018).
- Krajewska, B. Application of chitin and chitosan-based materials for enzyme immobilizations: a review. *Enzyme Microb. Technol.* **35**, 126–139 (2004).
- Payne, G. F. & Raghavan, S. R. Chitosan: a soft interconnect for hierarchical assembly of nano-scale components. *Soft Matter* **3**, 521–527 (2007).
- Liu, Y. et al. Biofabrication to build the biology-device interface. *Biofabrication* **2**, 022002 (2010).
- Cheng, Y. et al. In situ quantitative visualization and characterization of chitosan electrodeposition with paired sidewall electrodes. *Soft Matter* **6**, 3177–3183 (2010).
- Melke, J. et al. MetalSupport interactions of platinum nanoparticles decorated N-doped carbon nanofibers for the oxygen reduction reaction. *ACS Appl. Mater. Interfaces* **8**, 82–90 (2016).
- Zeng, D. W., Yung, K. C. & Xie, C. S. XPS investigation of the chemical characteristics of Kapton films ablated by a pulsed TEA CO₂ laser. *Surf. Coat. Technol.* **153**, 210–216 (2002).
- Diller, K. et al. Self-metalation of 2H-tetraphenylporphyrin on Cu(111): an x-ray spectroscopy study. *J. Chem. Phys.* **136**, 014705 (2012).
- Chen, Y. et al. Designed nitrogen doping of few-layer graphene functionalized by selective oxygenic groups. *Nanoscale Res. Lett.* **9**, 646 (2014).
- Ferrari, A. C. & Basko, D. M. Raman spectroscopy as a versatile tool for studying the properties of graphene. *Nat. Nanotechnol.* **8**, 235–246 (2013).
- Bukalov, S. S., Leites, L., Sorokin, I. a. & Kotosonov, a. S. Structural changes in industrial glassy carbon as a function of heat treatment temperature according to Raman spectroscopy and X-ray. *Nanosystems* **5**, 186–191 (2014).
- Socrates, G. *Infrared and Raman Characteristic Group Frequencies: Tables and Charts* (John Wiley & Sons, Chichester, West Sussex, England, 2004).
- Ortelli, E. E., Geiger, F., Lippert, T. & Wokaun, A. Pyrolysis of Kapton in air: an in situ DRIFT study. *Appl. Spectrosc.* **55**, 412–419 (2001).
- Dong, Y., Rismiller, S. C. & Lin, J. Molecular dynamic simulation of layered graphene clusters formation from polyimides under extreme conditions. *Carbon N. Y.* **104**, 47–55 (2016).
- Schaaf P. *Laser Processing of Materials: Fundamentals, Applications and Developments*, Vol. 139 (Springer Science & Business Media, Berlin, Heidelberg, 2010).

51. Ingram, J. M., Greb, M., Nicholson, J. A. & Fountain, A. W. Polymeric humidity sensor based on laser carbonized polyimide substrate. *Sens. Actuators B* **96**, 283–289 (2003).
52. Tiliakos, A., Ceaus, C., Iordache, S. M., Vasile, Eugeniu & Stamatina, I. Morphic transitions of nanocarbons via laser pyrolysis of polyimide films. *J. Anal. Appl. Pyrolysis* **121**, 275–286 (2016).
53. Jurkiewicz, K., Duber, S., Fischer, H. E. & Burian, A. Modelling of glass-like carbon structure and its experimental verification by neutron and X-ray diffraction. *J. Appl. Crystallogr.* **50**, 36–48 (2017).
54. Kumar, M. N., Muzzarelli, R. A., Muzzarelli, C., Sashiwa, H. & Domb, A. J. Chitosan chemistry and pharmaceutical perspectives. *Chem. Rev.* **104**, 6017–6084 (2004).
55. Warren, B. E. X-ray diffraction in random layer lattices. *Phys. Rev.* **59**, 693–698 (1941).
56. Brunauer, S., Emmett, P. H. & Teller, E. Adsorption of gases in multimolecular layers. *J. Am. Chem. Soc.* **60**, 309–319 (1938).
57. Lowell, S., Shields, J. E., Thomas, M. A. & Thommes, M. *Characterization of Porous Solids and Powders: Surface Area, Pore Size and Density*, vol. 16 (Springer Science & Business Media, Dordrecht, 2012).
58. Mamleyev, E. R. et al. Flexible carbon-based urea sensor by laser-induced carbonisation of polyimide. In *2018 International Flexible Electronics Technology Conference*, Ottawa, Canada, August 2018, <https://doi.org/10.1109/IFETC.2018.8583942> (2018).
59. Jakhar, S. & Pundir, C. S. Preparation, characterization and application of urease nanoparticles for construction of an improved potentiometric urea biosensor. *Biosens. Bioelectron.* **100**, 242–250 (2018).
60. Hu, C. Z. & Andrade, J. D. Pyrolyzed, conducting kapton polyimide: an electrically conducting material. *J. Appl. Polym. Sci.* **30**, 4409–4415 (1985).



Open Access This article is licensed under a Creative Commons Attribution 4.0 International License, which permits use, sharing, adaptation, distribution and reproduction in any medium or format, as long as you give appropriate credit to the original author(s) and the source, provide a link to the Creative Commons license, and indicate if changes were made. The images or other third party material in this article are included in the article's Creative Commons license, unless indicated otherwise in a credit line to the material. If material is not included in the article's Creative Commons license and your intended use is not permitted by statutory regulation or exceeds the permitted use, you will need to obtain permission directly from the copyright holder. To view a copy of this license, visit <http://creativecommons.org/licenses/by/4.0/>.

© The Author(s) 2019